Article

Dewetted Silver Nanoparticle-Dispersed WO₃ Heterojunction Nanostructures on Glass Fibers for Efficient Visible-Light-Active Photocatalysis by Magnetron Sputtering

Chadrasekhar Loka and Kee-Sun Lee*

Read Online

ACCESS | Metrics & More | Article Recommendations | SI Supporting Information

ABSTRACT: Fabrication of hybrid-heterojunction nanostructures comprising the Z-scheme and localized surface plasmon resonance is essential for enhancing the photocatalytic degradation of organic compounds to enable environmental remediation. This study focuses on the dispersion of dewetted Ag nanoparticles over the 3D network-like silica glass fibers (SGFs) coated with a Cu-doped WO₃ heterojunction system by a high-throughput and cost-effective method using magnetron sputtering, followed by solid-state dewetting. The influence of Cu doping on the crystal structure, growth direction, and morphology of WO₃ and the effect of localized surface diffusion-driven dewetted Ag nanoparticles on the photocatalytic performance were investigated. The Cu doping changed the optical band gap, and the 2Cu−WO₃/SGF exhibited excellent photocatalytic activity. The surface dispersion of dewetted Ag nanoparticles over Cu−WO₃/

SGFs exhibited lowest photoluminescence intensity, indicating the effective separation of photogenerated electrons−holes, which led to highest efficiency (~98%) in photocatalytic degradation of methylene blue among all the fibers with a degradation rate constant ($k = 0.0205$ min^{-1}) that was ~18.6 times higher than that of pure WO₃ ($k = 0.0011$ min^{-1}). The findings of this study can provide insights for designing low-cost and efficient visible-light-active photocatalysts for organic dye degradation, enabling environmental remediation.
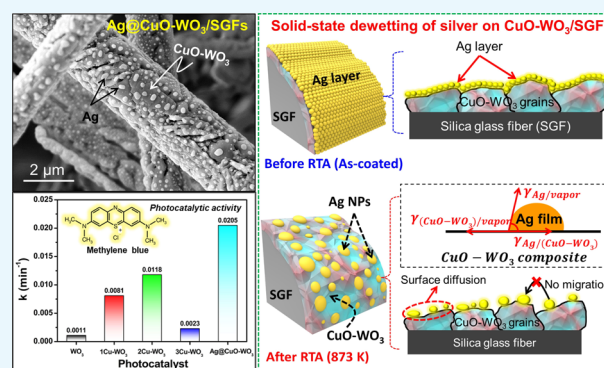
1. INTRODUCTION

The 21st century brought significant awareness about devastating environmental impacts and environmental consciousness in the society. Thus, the scientific community has developed substantial interest in the utilization of renewable energy, especially inexhaustible clean energy showered by the sun, for environmental remediation through the development of efficient visible-light-active photocatalysts to decontaminate air and water.[1,2] Tungsten oxide (WO₃) is a chemically stable non-toxic n-type semiconductor with a controllable optical band gap (2.4−2.9 eV) and good resistance against photocorrosion in aqueous media.[3] Therefore, WO₃ has potential applications in hydrogen production, virus deactivation, and harmful pollutant degradation,[4,5] which make it an appealing candidate for harvesting visible light to degrade organic compounds. However, the widespread application of WO₃ is inhibited due to the relatively low conduction band (CB) edge and the rapid recombination of photogenerated electrons and holes, which lead to poor photocatalytic reaction efficiency.[6] The photocatalytic efficiency can be significantly improved by improving the visible light absorption capacity, increasing the surface area, and reducing the recombination rate of photogenerated electron−hole pairs. To date, many scholars

have invested a lot of energy to accomplish enhanced photocatalytic activity of WO₃ by implementing various strategies such as doping, metal loading, and heterojunction formation.[7−9] Among them, the Z-scheme heterojunction system has attracted increasing attention, which promotes the separation of charge carriers in addition to possessing high redox ability.[9−11] Nevertheless, most of the existing Z-scheme photocatalysts are powder-based materials that often tend to agglomerate because of their high surface energy and involve complexities in the separation process of photocatalytic nanoscale powders from aqueous solutions. Moreover, these residues can cause secondary contamination. As a result, exploring the immobilized functional materials with high photocatalytic activity, which does not require any additional separation process, is easily recyclable, and low cost is imperative for advanced and sustainable photocatalysis. In
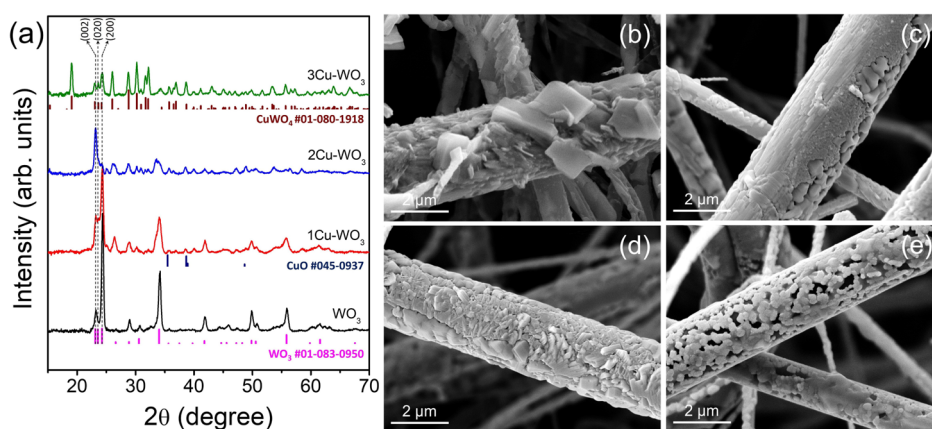
Figure 1. (a) XRD spectra of WO_3 and $Cu-WO_3$-coated SGFs annealed at 873 K; FE-SEM images (magnification: 30 000×) of (b) WO_3, (c) $1Cu-WO_3$-, (d) $2Cu-WO_3$-, and (e) $3Cu-WO_3$-coated SGFs annealed at 873 K.

this context, it is expected that the exploitation of network-like fibers as a substrate material or a supporting skeleton for the photocatalyst could be a viable solution for environmental friendliness. The fibers possess potential advantages such as good adsorption ability, high surface area, good physicochemical and thermal stability, low cost, reusability, and recyclability.[12] Fukugaichi reported TiO_2 nanoparticle (NP) dispersions on glass fibers with enhanced photocatalytic degradation of organic dyes.[13] Heo et al. exploited filter fibers for antimicrobial applications using TiO_2 nanoparticle coverage through a simple aerosol deposition method, which is impressive in this COVID-19 pandemic situation.[14]

Recently, the mere dispersion of plasmonic metal nanoparticles (such as Ag, Au, Cu, Pt, and Pd) onto a dielectric surface that can radically alter the localized surface plasmon resonance (LSPR) has been considered as the state of the art in the areas of photocatalysis, surface-enhanced Raman scattering, plasmon-enhanced fluorescence, photovoltaics, chemical, and biological sensing applications.[15,16] However, fabrication of these nanoparticles with appropriate structure, size, density, and arrangement is crucial as they influence the LSPR phenomenon. To date, chemical synthesis and lithography were reported to fabricate plasmonic metal nanoparticles,[17,18] which have limitations such as high cost, complexity in processing, high temperature, reproducibility, and time-consuming. In addition, most of these studies reported on the preparation of both patterned and randomly arranged nanoparticles on flat substrates rather than non-flat substrates. Silver has unique advantages over other plasmonic metals, such as low cost, bactericidal properties, high work function, and special behavior for oxygen adsorption.[19] Moreover, the dispersion of evenly distributed plasmonic Ag nanoparticles improves the visible light absorption range, in addition to substantially ameliorating the photocatalytic degradation efficiency of organic pollutants, by suppressing electron–hole recombination.[20] The loading of Ag on metal oxides was generally achieved by photoreduction, conventional impregnation, or chemical reduction methods for photocatalysis.[21–23] Solid-state dewetting, a spontaneous physical phenomenon that refers to the decomposition of a thin film into small particles or nanostructures, leaving voids on a substrate, driven by excess energy due to high fraction of grain boundaries, interfaces, surfaces, or residual stresses is another approach for the dispersion of Ag nanoparticles.[24–26] Although solid-state dewetting is the simplest method, the template or

seed-mediated patterning is inevitable,[15,17,18] which again involves complex processing (such as lithography/shadow-mask and so forth) for the 3D network-like substrates.

In this work, we report the fabrication of evenly dispersed Ag nanoparticles with a high-throughput and cost-effective method using magnetron sputtering, followed by solid-state dewetting. To the best of our knowledge, Ag dewetting-driven homogeneous Ag nanoparticle dispersion over 3D network-like fibers has rarely been reported. Utilization of low-cost, reusable, and recyclable 3D-network-like silica glass fibers (SGFs) as supporting materials and the preparation of hybrid nanostructures $CuO-WO_3$/SGF and Ag nanoparticle dispersion based on the Z-scheme and LSPR phenomena for high-performance, practicable, visible-light-active photocatalysts are demonstrated. CuO is a direct band gap p-type semiconductor photocatalyst with a band gap of 1.3–1.7 eV, which is mostly coupled with other semiconductors to form a heterojunction that can potentially inhibit the recombination of photogenerated electron–hole pairs.[27,28] In this work, the synergistic properties arising from the hybrid nanostructure composed of $CuO-WO_3$ composite coated on SGFs and the solid-state dewetting-driven surface dispersion of Ag nanoparticles are thoroughly investigated for an efficient visible-light-active photocatalyst.

2. RESULTS AND DISCUSSION

2.1. Crystal Structure and Microstructural Changes in $Cu-WO_3$ Fibers.
Figure 1a shows the X-ray diffraction (XRD) results of the undoped and Cu-doped WO_3-coated fibers annealed at 873 K. The undoped WO_3 fibers exhibited a monoclinic-WO_3 phase (JCPDS no. 01-083-0950) with characteristic peaks of (002), (020), and (200) facets at 2θ = 23.11, 23.55, and 24.24°, respectively. Among these three characteristic peaks, the (200) facet exhibited high intensity, indicating the preferred direction of growth. The $1Cu-WO_3$ and $2Cu-WO_3$ fibers also exhibited a monoclinic WO_3 phase (JCPDS no. 01-083-0950). However, with increasing Cu concentration, the crystal structure and growth direction of WO_3 significantly changed. The XRD intensity of the (002) peak increased with increasing Cu concentration, whereas the intensity of the (200) peak decreased. The change that occurred in the preferred orientation of WO_3 could be explained as follows: the as-coated fibers exhibited an amorphous phase (data not shown here), which recrystallized during the rapid thermal annealing (RTA) through surface
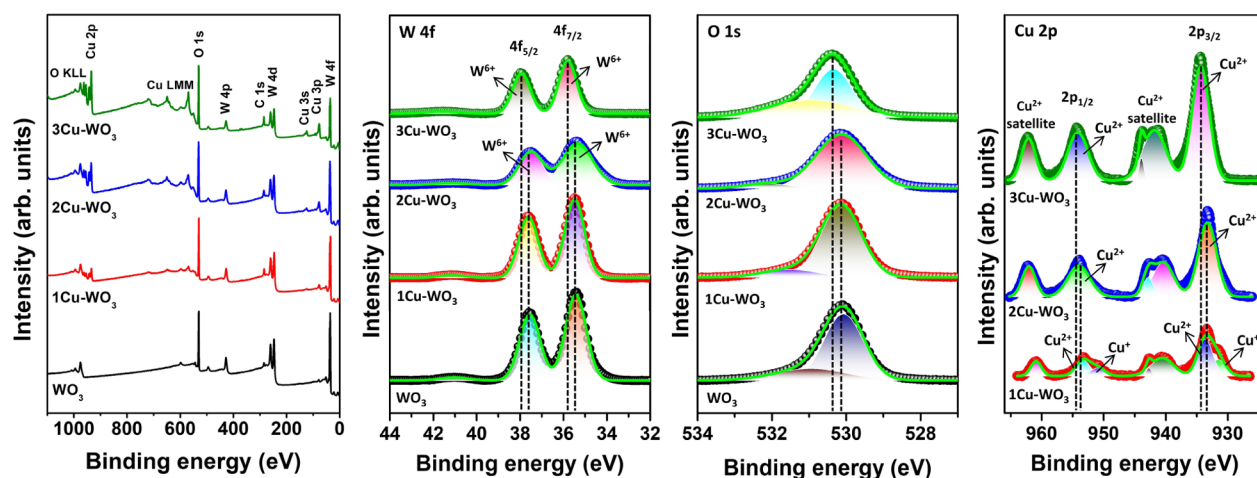
Figure 2. XPS survey spectra and high-resolution spectra of WO$_3$ and Cu−WO$_3$-coated SGFs annealed at 873 K.

reconfiguration, by evolving the crystal planes with low surface energy to lower the total surface energy. The literature suggested that the surface energies of monoclinic WO$_3$ followed the order (002) > (020) > (200) with corresponding surface energies of 1.56 > 1.54 > 1.43 J/m^2, which implied that the (200) plane was a highly stable phase, while the (002) plane was unstable.[29] Among the three characteristic facets (002), (020), and (200) of WO$_3$, the (002) facet was reported to exhibit significantly enhanced adsorption of reactive species during the photocatalytic reaction in comparison with the other facets.[30] Cu doping could be effective for the recrystallization of the Cu−WO$_3$ fibers in the (002) plane, which became predominant in 2Cu−WO$_3$. A similar observation was reported by Kalanur and Seo where the WO$_3$-preferred orientation was systematically tuned by controlling the Al doping;[30] a higher concentration of dopant changed the crystal structure, as the dopant took W positions in the lattice and was distributed uniformly throughout the crystal structure. Therefore, a further increase in the Cu content revealed the formation of the triclinic CuWO$_4$ (JCPDS no. 01-080-1918) phase due to the replacement of W by Cu in the lattice to form the CuWO$_4$ phase. All the Cu−WO$_3$-coated fibers annealed at 873 K exhibited XRD peaks at 2θ of 35.5 and 38.6° attributed to the (−111) and (111) planes of the monoclinic CuO phase (JCPDS no. 45-0937), and a gradual increase in the CuO peak intensity was observed with an increase in Cu content. It has been reported that the thermodynamic equilibrium oxide phase (Cu−O) was wholly determined by the applied oxidation temperature, rather than growth kinetics, and as a result, CuO phase formation was ensured because of rapid O$_2$ diffusion above its critical temperature of 600 K.[31,32] Thus, in this study, a higher oxidation temperature (873 K) could drastically enhance the O$_2$ diffusion process to form CuO. Consequently, the XRD results revealed that the 1Cu−WO$_3$- and 2Cu−WO$_3$-coated fibers annealed at 873 K comprised the WO$_3$ and CuO composite phases, and the 3Cu−WO$_3$ fibers consisted of CuWO$_4$ and CuO composite phases.

The surface morphologies of the undoped and Cu-doped WO$_3$-coated fibers annealed at 873 K were observed by field-emission scanning electron microscopy (FE-SEM), as shown in Figure 1b−e. The as-coated fibers are shown in Figure S1, where all the fibers were aligned like the 3D network, with the existence of macropores; they exhibited a glossy and

homogeneous surface morphology. As shown in Figure 1b, the pure WO$_3$-coated fibers exhibited a flake-like surface microstructure and the formation of a few nanoplates with well-grown facets and sharp facet edges, which indicated the typical morphology of the crystalline WO$_3$ nanoplates. The 1Cu−WO$_3$ and 2Cu−WO$_3$ fibers exhibited densely covered large grains that could be composed of the CuO−WO$_3$ composite as shown in Figure 1c,d, respectively. In addition, the 3Cu−WO$_3$ fibers exhibited a porous microstructure and agglomerated grains. It could be understood that in the case of high-concentration Cu-doped WO$_3$ fibers, the Cu atoms could rapidly diffuse into the adjacent WO$_3$ phase during the RTA process to occupy the W atom sites.[33] This would lead to the formation of localized pores, as shown in Figure 1e, forming the CuWO$_4$ phase, as confirmed by the XRD results.

2.2. Chemical Composition and Optical Properties of Cu−WO$_3$ Fibers. X-ray photoelectron spectroscopy (XPS) measurements were conducted to investigate the surface chemical composition and state of the WO$_3$ and Cu−WO$_3$-coated fibers annealed at 873 K. As shown in Figure 2, the survey spectrum showed the peaks of W, Cu, and O in Cu−WO$_3$-coated fibers. With an increase in Cu concentration, the Cu−WO$_3$ fibers exhibited a very intense signal of Cu along with the presence of strong satellite peaks, and the W signal was significantly decreased. The high-resolution W 4f spectra of WO$_3$, 1Cu−WO$_3$, and 2Cu−WO$_3$ were deconvoluted into three peaks with binding energies of 35.4, 37.5, and 41.0 eV, corresponding to W 4f$_{7/2}$, W 4f$_{5/2}$, and the satellite peak of WO$_3$, respectively, which were consistent with the W^{6+} state.[34] Moreover, the splitting energy of the W 4f doublet at 2.1 eV also confirmed the W^{6+} state. The peak at 41.0 eV could be attributed to the binding energy of W 5p$_{3/2}$.[35,36] However, a slight shift in the W 4f spectra toward a higher energy of about 0.4 eV for 3Cu−WO$_3$ was observed, which is in good agreement with a similar observation reported by Thongpan et al. for the CuWO$_4$ phase.[37] The W 4f spectra of 3Cu−WO$_3$ were fitted into two peaks at 35.8 and 37.9 eV corresponding to W 4f$_{7/2}$ and W 4f$_{5/2}$ of W^{6+} in the form of CuWO$_4$, respectively. The deconvolution of high-resolution XPS spectra of Cu 2p for 1Cu−WO$_3$ and 2Cu−WO$_3$ showed that two major peaks centered at 933.65 and 953.45 eV are assigned to Cu 2p$_{3/2}$ and Cu 2p$_{1/2}$ of Cu^{2+}, respectively, which confirmed the CuO phase.[38,39] The binding energy difference between the two peaks Cu 2p$_{3/2}$ and Cu 2p$_{1/2}$ was 19.8 eV, which

strongly indicated the presence of Cu^{2+}.[40] In addition, the presence of strong satellite peaks around 940−944 and 962 eV in the Cu−WO$_3$/SGFs corresponds to Cu 2p$_{3/2}$ and Cu 2p$_{1/2}$, respectively, which indicate an open Cu 3d^9 shell corresponding to the bivalent (Cu^{2+}) state (CuO phase).[27,39,40] However, the peaks centered at 931.6 and 951 eV are attributed to Cu 2p$_{3/2}$ and Cu 2p$_{1/2}$ of Cu$^+$,[41] which indicates the presence of a small amount of Cu$_2$O phase in the 1Cu−WO$_3$-coated fibers. The relative concentrations of Cu$^+$ and Cu^{2+} species present on 1Cu−WO$_3$ was quantified to be about 18% (Cu$^+$) and 82% (Cu^{2+}) by considering the curve-fitting of the total Cu 2p emission peaks including the shake-up satellite peaks as reported by Biesinger et al. using the following equations[42,43]

$$\% \ Cu^+ = A2/(A + B) \times 100$$

$$\% \ Cu^{2+} = (B + A1)/(A + B) \times 100$$

where B is the area of the shake-up peak and A is the total area of the Cu 2p main peak. The main emission line (A) contains both Cu^{2+} ($A1$) and Cu$^+$ ($A2$) contributions, but the satellite intensity (B) is entirely from Cu^{2+}.[42] In the case of 3Cu−WO$_3$, the Cu 2p peaks were slightly shifted (about 0.7 eV) toward higher binding energies, and they were deconvoluted into two major peaks centered at 934.4 and 954.2 eV, attributed to Cu 2p$_{3/2}$ and Cu 2p$_{1/2}$, respectively, due to Cu^{2+} in the lattice sites of CuWO$_4$.[44] The observed peak shifting in the Cu 2p spectra of the CuWO$_4$ phase is in good agreement with the previous reports.[45] The O 1s exhibited peaks at about 531 and 530 eV in both WO$_3$ and Cu−WO$_3$ fibers, which were attributed to the surface-adsorbed oxygen and the characteristic peak of metal ion-associated oxygen (W−O and Cu−O), respectively.[46]

Raman spectroscopy is a well-known non-destructive method that is commonly used to investigate material properties including the structure and phase change owing to its high sensitivity to the electronic structure. Therefore, Raman spectroscopy was further utilized to evaluate the chemical bonds of Cu−WO$_3$. The Raman spectra displayed in Figure 3 revealed five active modes in 1Cu−WO$_3$ and 2Cu−WO$_3$/SGF centered at about 134, 272, 326, 712, and 806 cm^{-1}. The peak that appeared at 134 cm^{-1} is ascribed to the lattice vibration of WO$_3$; 272 and 326 cm^{-1} are assigned to the δ(O−W−O) bending modes. The other two peaks centered at 712 and 806 cm^{-1} correspond to the ν(O−W−O) vibrational
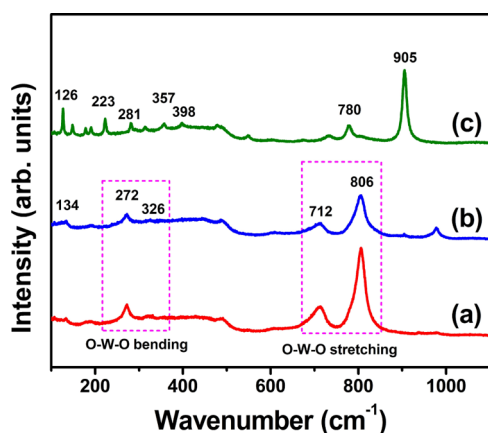
Figure 3. Raman spectra of the Cu−WO$_3$/SGFs annealed at 873 K: (a) 1Cu−WO$_3$, (b) 2Cu−WO$_3$, and (c) 3Cu−WO$_3$.

stretching modes of the monoclinic WO$_3$.[47,48] The peak at 978 cm^{-1} in the 2Cu−WO$_3$/SGF is attributed to the symmetric stretching mode of W=O bonds resulting from the adsorbing water molecules in the air.[37] Based on group theory calculations, the triclinic CuWO$_4$ exhibits 36 vibrational modes ($\Gamma_{Raman+infrared} = 18A_g + 18A_u$).[49] For the 3Cu−WO$_3$/SGF, we have observed different Ag active Raman modes, among which the highest intense peak is observed at about 905 cm^{-1}, which is ascribed to the W−O stretching vibration $\nu_1(A_g)$. The other peaks, 313 cm^{-1} attributed to the scheelite tungstate vibration $\nu_2(A_g)$ in the triclinic lattice and 780 cm^{-1} associated with the scheelite structure vibration $\nu_3(A_g)$, confirm the triclinic CuWO$_4$ phase.[50] The peaks at 357 and 398 cm^{-1} correspond to the deformation modes of $r(B_g)$ and $\delta(A_g)$, respectively. The Raman peaks observed in 3Cu−WO$_3$-coated fibers are in good coincidence with the previous reports of the CuWO$_4$ phase.[50] Consequently, the Raman spectroscopy studies are well corroborated with the XRD and XPS results, which confirm that the higher doping concentration of Cu leads to CuWO$_4$ phase formation.

Visible light absorption was an important precondition for efficient visible-light-active photocatalysts. Figure 4 shows the
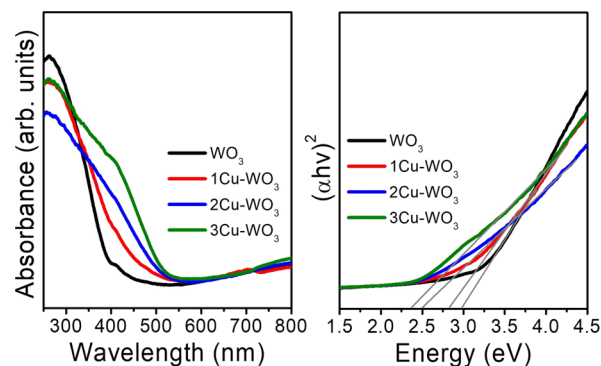

Figure 4. UV−visible absorption spectra and Tauc's plot of undoped and Cu-doped WO$_3$ structures annealed at 873 K.

UV−visible absorption spectra of the WO$_3$ and Cu−WO$_3$-coated fibers annealed at 873 K. The absorption spectra vary with Cu doping. It was observed that the red shift in the absorption spectra occurred with an increase in the Cu content, which was favorable for visible light photocatalysis. The optical band gaps of the WO$_3$ and Cu−WO$_3$ fibers were determined using Tauc's equation as follows

$$\alpha h\vartheta = A(h\vartheta - E_g)^n$$

where α is the absorption coefficient, $h\vartheta$ is the incident photon energy, A is an arbitrary coefficient, n = 1/2 for direct and n = 2 for indirect recombination, and E_g is the optical band gap. The optical band gap of WO$_3$, 1Cu−WO$_3$, 2Cu−WO$_3$, and 3Cu−WO$_3$ was determined to be approximately 2.95, 2.82, 2.51, and 2.36 eV, respectively, by the linear extrapolation of Tauc's plot $(\alpha h\vartheta)^2$ versus $h\vartheta$ (Figure 4). The variation in the optical band gap implied that Cu doping reduced the optical band gap, which was significant for visible-light-active photocatalysis. Similar observations were reported for Cu-doped WO$_3$.[51] Narrowing the band gap was presumed to enhance the absorbance of visible light. The 3Cu−WO$_3$ fibers showed the lowest band gap among all the fibers (~2.36 eV), which was due to the formation of CuWO$_4$, as confirmed from the XRD results. Moreover, the obtained band gap of 3Cu−WO$_3$ was in
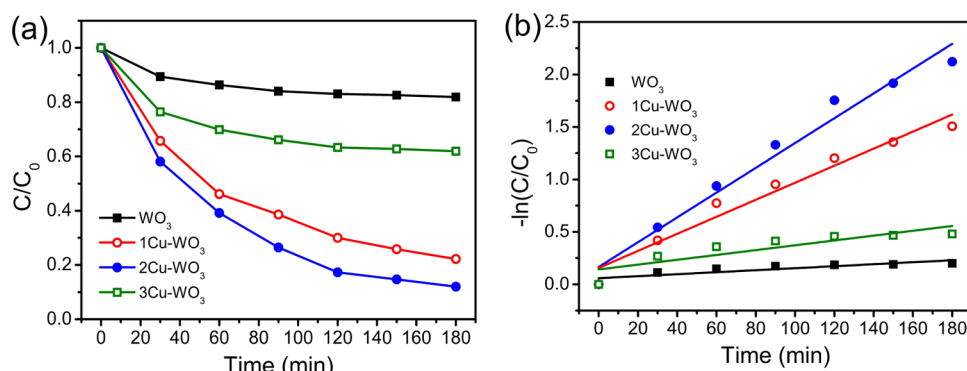
Figure 5. (a) Change in concentration vs reaction time for the degradation of MB solution under visible light irradiation and (b) MB degradation kinetics of the WO_3 and $Cu-WO_3$-coated SGF.
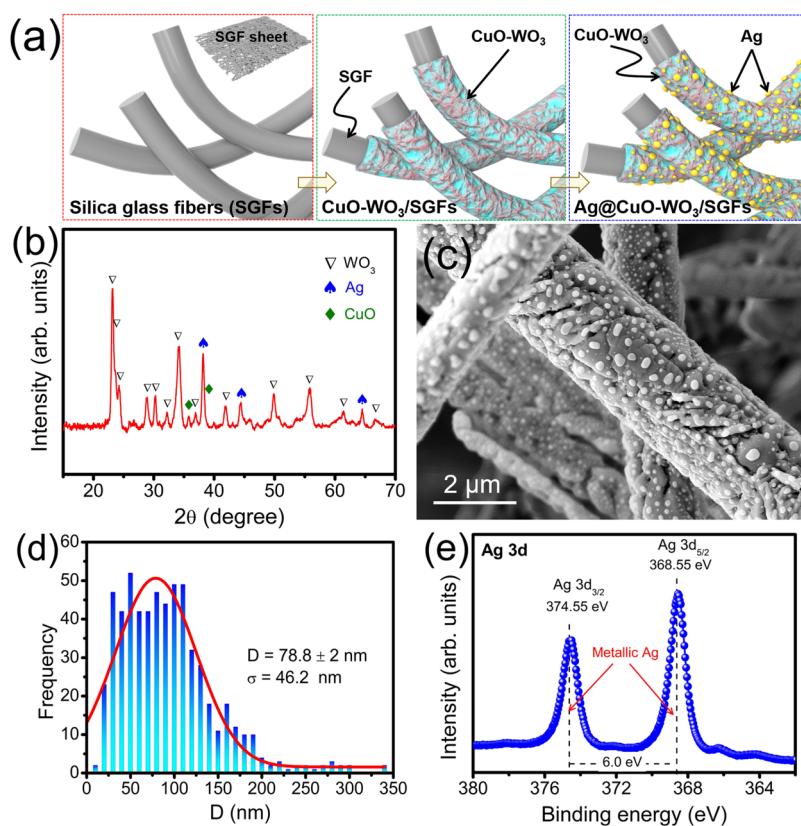

Figure 6. (a) Schematic illustration of the fabrication of Ag-dispersed $CuO-WO_3$/SGFs (Ag@CuO−WO$_3$/SGFs), (b) XRD pattern, (c) high-magnification (30 000×) FE-SEM surface morphology of Ag-dispersed $CuO-WO_3$, (d) Ag nanoparticle distribution histogram, and (e) high-resolution XPS spectra of Ag 3d of Ag-dispersed $CuO-WO_3$.

agreement with the other reports on $CuWO_4$ nanostructures, whose band gap was approximately 2.3 eV.[52,53]

2.3. Photocatalytic Activity of Cu−WO$_3$ Fibers. The photocatalytic activities of the WO_3 and $Cu-WO_3$-coated fibers annealed at 873 K were evaluated through methylene blue (MB) degradation under visible light irradiation. As shown in Figure 5a, it could be distinctly observed that the $2Cu-WO_x$ fibers exhibited the highest efficiency of photocatalytic degradation compared to other fibers. The undoped WO_3 fibers degraded about 18.5%, and $2Cu-WO_3$ fibers degraded 88.0% of MB in 180 min. It is known that the efficiency of photogenerated electron−hole pair separation plays a crucial role in increasing the photocatalytic degradation rate of the organic dye. Langmuir−Hinshelwood's first-order

kinetic model was used to determine the photocatalytic activity for MB degradation as follows[54]

$$-\ln\left(\frac{C}{C_0}\right) = kt$$

where C_0 is the initial concentration of MB and C is the concentration of MB in the presence of fibers after visible light exposure. The MB degradation kinetics of undoped WO_3 and $Cu-WO_3$ fibers are shown in Figure 5b, and the fitted data exhibited a linear behavior for all the fibers, indicating that the MB degradation reactions followed the pseudo-first-order kinetics model. The photocatalytic activity rate constants (k) of WO_3, $1Cu-WO_3$, $2Cu-WO_3$, and $3Cu-WO_3$ fibers were 0.0011, 0.0081, 0.0118, and 0.0023 min^{-1}, respectively. The

WO_3-coated fibers exhibited the lowest rate constant, which could be due to rapid electron–hole recombination. The 2Cu–WO_3 fibers exhibited approximately 10.7 times higher activity rate constant than pure WO_3. In fact, the CB of WO_3 is more positive than the $O_2/O_2^{\bullet-}$ redox potential (−0.33 eV), which indicates that the adsorbed O2 molecules on the surface of WO_3 cannot be reduced to superoxide radicals $O_2^{\bullet-}$. The valence band (VB) of CuO (+1.43 eV) is less positive than $OH^-/^{\bullet}OH$ (+2.38 eV), which indicated that CuO could not directly produce the $^{\bullet}OH$ radicals. Hence, the observed enhanced photocatalytic activity could not be explained by the conventional p–n heterojunction formation of CuO–WO_3. A more credible mechanism could be the Z-scheme heterojunction formation; in the case of Cu–WO_3 samples, the photogenerated electrons from the CB of WO_3 could recombine with the holes in the VB of CuO. As the CB of CuO was more negative than the redox potential, the electrons could participate in the redox reactions to form the superoxide radical $O_2^{\bullet-}$. The holes in WO_3 could contribute to the oxidation process to produce the $^{\bullet}OH$ radicals because the VB of WO_3 was more positive than the oxidation potential to yield $^{\bullet}OH$. Thus, the electrons in the CB of CuO and holes in the VB of WO_3 could effectively perform redox/oxidation reactions. 2Cu–WO_3 possessed a higher concentration of Cu than 1Cu–WO_3. This led to the formation of higher phase fraction of CuO while forming the CuO/WO_3 interfaces. This resulted in higher photocatalytic activity. Thus, the enhanced photocatalytic activity conformed to the CuO–WO_3 Z-scheme heterojunction mechanism, which greatly enhanced the separation of photogenerated electrons–holes. Moreover, the (002) crystal orientation of WO_3 in 2Cu–WO_3 predominantly accelerated the transfer of photoinduced charge carriers to ascertain high reactivity, compared to other orientations, as reported by several researchers.[55,56] It is to be noted that the surface area of the photocatalyst greatly influenced the photocatalytic activity; herein, the 3D network-like fiber substrates obviously possess a high surface area compared to the 2D substrates. In the case of 3Cu–WO_3 fibers, the lower photocatalytic activity could be due to the $CuWO_4$ phase formation and porosity, which could be attributed to the smaller volume fraction of CuO. In general, the $CuWO_4$ phase has a CB edge of approximately 0.2–0.44 V versus NHE, which is more positive than the O_2 reduction potential;[57] hence, the lower photocatalytic activity can be obviously observed in 3Cu–WO_3 fibers. Overall, the 2Cu–WO_3-coated fibers exhibited better photocatalytic activity among the Cu–WO_3-coated SGFs.

2.4. Silver Dewetting on CuO–WO_3 Fibers.

Ag nanoparticles were dispersed over CuO–WO_3 (2Cu–WO_3) fibers to further enhance the photocatalytic activity of the fibers, as shown in Figure 6a. A 10 nm-thick Ag film was sputtered on the CuO–WO_3 fibers and subsequently vacuum-annealed by RTA at 873 K for 5 min to obtain the island formation and growth of Ag in the form of isolated nanoparticles. The crystal structure of the Ag-dispersed CuO–WO_3 fibers was studied by XRD, as shown in Figure 6b. The XRD peaks observed at 38.2, 44.4, and 64.6 were attributed to the (111), (200), and (220) planes of silver (JCPDS no. 01-087-0720). In addition, the other peaks were similar to the diffraction pattern observed in 2Cu–WO_3 composed of the CuO–WO_3 composite phase, where the most intense peak of the (002) facet was observed, indicating that the growth of the WO_3 crystal was along the [001]

direction. The high-magnification (30 000×) surface microstructure of the Ag-dispersed CuO–WO_3 fibers clearly indicated the formation of evenly distributed Ag nanoparticles over the surface of CuO–WO_3, as shown in Figure 6c. The corresponding low-magnification (5000×) image is shown in Figure S2. The size distribution histogram of the Ag nanoparticles is shown in Figure 6d, where the solid line represents the Gaussian fitting to a normal distribution curve. Based on this fitting, the mean size (D) and standard deviation (σ) of the Ag nanoparticles were 78.8 ± 3 and 46.2 nm, respectively. The surface coverage of the Ag nanoparticles was determined to be approximately 24.9% using ImageJ software. The high-resolution XPS spectrum of Ag 3d is shown in Figure 6e, where two peaks with binding energies centered at 368.55 and 374.55 eV were observed with an energy gap of 6.0 eV, which corresponded to Ag $3d_{5/2}$ and Ag $3d_{3/2}$ of metallic Ag, respectively.[58] This result was in good accordance with the results from the XRD analysis, indicating the metallic nature of Ag.

Additional structural information of Ag-dispersed CuO–WO_3 fibers was examined using high-resolution transmission electron microscopy (HR-TEM), and TEM sampling was performed using the focused ion beam (FIB) H-bar technique, as shown in Figure 7a. Before milling, the surface of the target
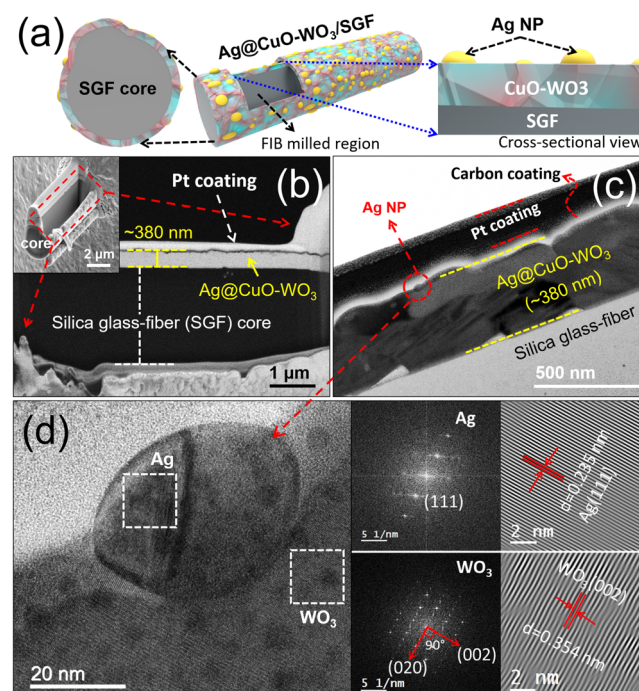

Figure 7. (a) Schematic cross-sectional view of the Ag-dispersed CuO–WO_3/SGF and the FIB-milled TEM sampling, (b) BSE SEM micrographs of FIB-milled Ag-dispersed CuO–WO_3 fiber cross-sectional view, (c) TEM cross-sectional micrograph, and (d) HR-TEM image of the Ag-dispersed CuO–WO_3/SGF.

region of the Ag-dispersed CuO–WO_3 fiber was coated with a thin carbon layer, followed by a platinum protective coating to avoid milling of the target region. Milling was performed with a high-energy Ga ion beam. The milled specimen was picked and mounted on a TEM specimen grid. Subsequently, the specimen was milled again to obtain a very thin piece (electron transparent) with a sample thickness of less than 100 nm. The backscattered electron (BSE) images of the high-

energy milled specimen (inset of Figure 7b) and final sample preparation (the rectangular region shown in the inset) are shown in Figure 7b. The cross-sectional TEM image (Figure 7c) shows the existence of Ag nanoparticles on the surface, and the thickness of the Ag-dispersed CuO−WO$_3$ coating was approximately 380 nm. From the HR-TEM image (Figure 7d), a small near-spherical silver nanoparticle in the range of ∼50 nm was observed, which formed an interface with the monoclinic WO$_3$ phase. The crystal structure of silver was determined by the lattice fringes, and the corresponding fast Fourier transformation (FFT) and inverse FFT (IFFT) images of the marked region are depicted in Figure 7d. The interplanar distance of the lattice fringes was determined to be d = 0.235 nm, which corresponded to the d-spacing of the Ag(111) plane. Similarly, the FFT and IFFT images of WO$_3$ are shown in Figure 7d, which corresponded to monoclinic WO$_3$ with an interplanar distance d = 0.354 nm of the (002) plane. Based on the above results, Ag nanoparticle dispersion through Ag solid-state dewetting was successfully obtained. As shown in the schematic in Figure 8, the as-deposited Ag layer
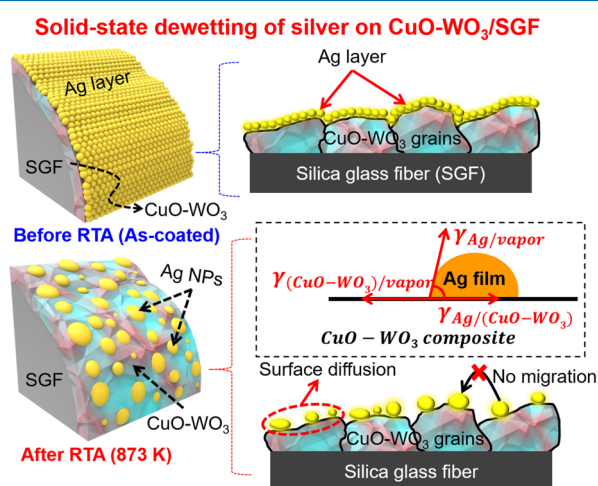

Figure 8. Cross-sectional and plane-view schematic representation for before and after RTA of a thin Ag layer-coated CuO−WO$_3$/SGF, illustrating the localized surface diffusion-driven Ag dewetting (3D island-like Ag nanoparticle formation).

on the CuO−WO$_3$-coated fibers comprised numerous Ag adatoms. When subjected to RTA, the interfacial free energy between Ag and CuO−WO$_3$ spontaneously induced the separation and isolation of Ag (Ag solid-state dewetting). More specifically, from a thermodynamic point of view, dewetting occurred when the surface energy (E_s) was positive, and the driving force was defined as follows

$$E_s = \gamma_{Ag} + \gamma_{Ag,(CuO−WO_3)} − \gamma_{(CuO−WO_3)}$$

where γ_{Ag}, $\gamma_{(CuO−WO_3)}$, and $\gamma_{Ag(CuO−WO_3)}$ are the surface energy densities of Ag, CuO−WO$_3$, and Ag and CuO−WO$_3$, respectively. The evolution of isolated Ag nanoparticles in an Ag thin film sputtered on a glass substrate is depicted in Figure S3 for clearly understanding the formation of the Ag dewetting-induced Ag nanoparticle. The as-deposited Ag layer showed unstable or metastable Ag adatoms with a relatively smooth microstructure, which was ascribed to insufficient surface diffusion to obtain a low-energy configuration. The Ag adatoms started to diffuse on the surface with an increase in temperature and finally formed isolated island-

like spherical or near-spherical nanoparticles owing to the lower surface energy. Surface diffusion was the major driving parameter for the Ag dewetting behavior, and the diffusion coefficient (D_s) of the atom could be related to the temperature (T) as follows[25]

$$D_s = D_0 \, \exp\left(-\frac{E_a}{kT}\right)$$

where D_0 is the pre-exponential factor of the surface diffusion coefficient, E_a is the activation energy, k is the Boltzmann constant, and T is the applied temperature. From the above equation, it is obvious that D_s is related to T. In the process of surface diffusion, voids were eventually formed, and the growth rate of the surface diffusion-induced voids accelerated with temperature.[59] Thus, the surface diffusion coefficient increased with an increase in temperature, which indicated that the Ag adatoms had a high probability of coalescence with the adjacent atoms to form a 3D island-like nanoparticle. In addition, the Ag nanoparticle density decreased, and the voids grew larger. The 873 K annealed films exhibited homogeneously distributed Ag island-like nanoparticles. As the CuO−WO$_3$-coated fibers were composed of large grains and a seemingly rough surface, the Ag nanoparticle growth was physically limited to each grain of the substrate (CuO−WO$_3$ surface), and they could not physically migrate (hopping) from one grain to another, as illustrated in the schematic in Figure 8. As a result, the formation of large nanoparticles, unlike the Ag nanoparticles which formed over a flat and smooth surface (for instance, glass substrate), was restrained. Therefore, in the case of CuO−WO$_3$-coated fibers, small island-like Ag nanoparticles were formed owing to the localized surface diffusion-driven Ag dewetting, as observed in the FE-SEM image (Figure 6c).

2.5. Influence of Dewetted Ag NPs on Photocatalytic Activity. The photocatalytic activity and MB degradation kinetics of the Ag-loaded CuO−WO$_3$ fibers are shown in Figure 9a. It was observed that 58% of MB was decomposed within the first 30 min and 98% degradation was observed after 180 min, which was much higher than that of the Cu−WO$_3$ fibers. The photocatalytic activity rate constant of WO$_3$, Cu−WO$_3$, and Ag-dispersed CuO−WO$_3$ fibers is shown in Figure 9b, where the Ag-dispersed CuO−WO$_3$ fibers exhibited remarkable photocatalytic activity among all the fibers with the highest MB degradation rate constant (k = 0.0205 min^{-1}), which is approximately 1.73 times higher than that of 2Cu−WO$_3$ fibers and 18.6 times higher than that of pure WO$_3$. The photocatalytic MB degradation stability of the Ag-dispersed CuO−WO$_3$ fibers was determined under the identical conditions and shown in Figure S4. The efficiency was slightly changed with the degradation efficiency of about 90% during the third cycling, while the first cycling experiment showed about 98% efficiency. The XRD pattern and the FE-SEM image of the Ag@CuO−WO$_3$ sample after the photocatalytic MB degradation stability test for the third cycling are shown in Figure S5.

The photocatalytic efficiency relies critically on the generation and recombination rates of electron−hole pairs upon light excitation. Photoluminescence (PL) spectroscopy is an important characterization tool for the investigation of surface processes involving photogenerated electron−hole pair recombination in semiconductors. The lower PL intensity implied more effective separation of electron−hole pairs; thus, higher photocatalytic activity could be achieved. PL was
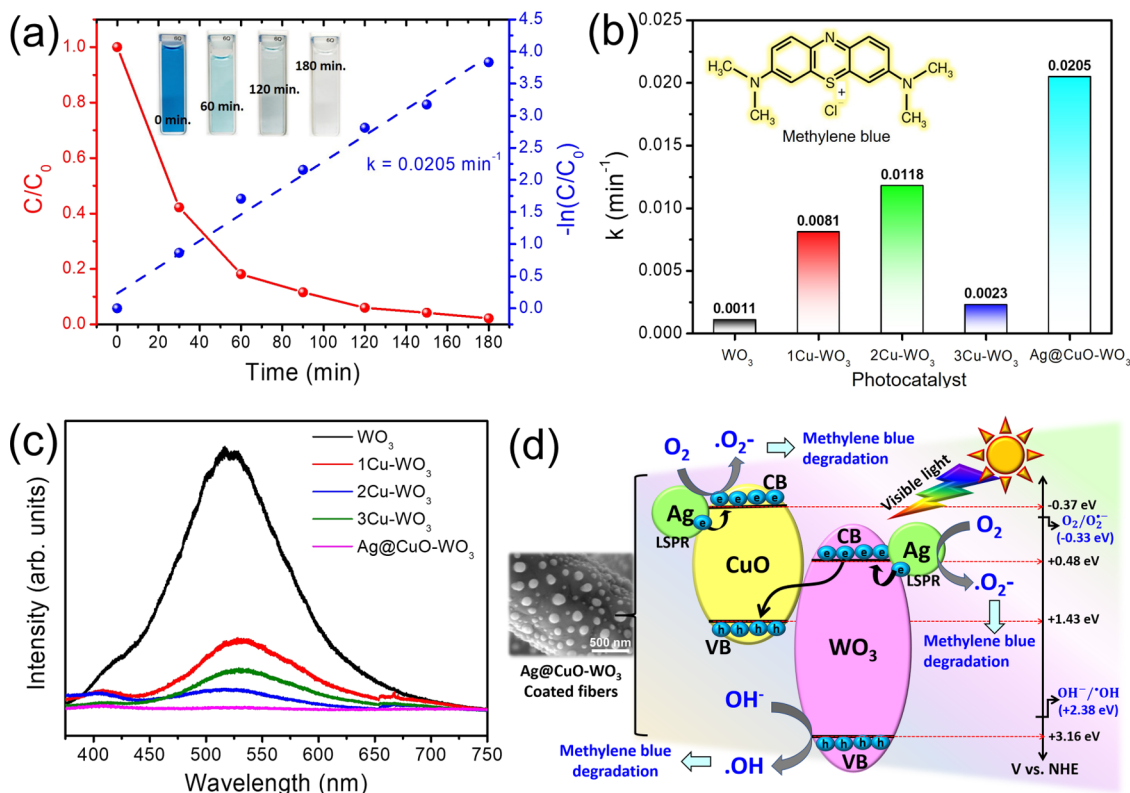
Figure 9. (a) Photocatalytic activity of Ag-dispersed CuO−WO$_3$; (b) MB degradation rate constant of WO$_3$, Cu−WO$_3$, and Ag-dispersed CuO−WO$_3$ photocatalysts; (c) PL spectra of the WO$_3$, Cu−WO$_3$, and Ag-dispersed CuO−WO$_3$/SGF; and (d) schematic illustration of the proposed LSPR and Z-scheme hybrid heterojunction mechanism in the Ag-dispersed CuO−WO$_3$/SGF photocatalyst.

measured for WO$_3$, Cu−WO$_3$, and Ag-dispersed CuO−WO$_3$ fibers, as shown in Figure 9c, and the fibers showed emission peaks around 530 nm. The pure WO$_3$ fibers exhibited the strongest PL intensity due to the severe electron−hole recombination, while the Cu-doped WO$_3$ fibers exhibited lower PL intensity than WO$_3$. 2Cu−WO$_3$ exhibited the lowest PL intensity among all the Cu-doped WO$_3$ fibers, indicating the effective retardation of electron−hole recombination. The PL intensity drastically decreased in Ag-dispersed CuO−WO$_3$ fibers, which indicated that Ag loading greatly inhibited the recombination rate of the electron−hole pairs, resulting in effective charge separation at the respective interfaces of Ag/CuO/WO$_3$. The mechanism for the enhanced photocatalytic activity of the Ag-dispersed CuO−WO$_3$ fibers could be understood as follows: the schematic is shown in Figure 9d on the synergetic effect of the Z-scheme and LSPR. The fast electron−hole pair recombination rate was greatly inhibited by the Z-scheme system of CuO−WO$_3$, and the strong LSPR effect of dewetted Ag nanoparticles functions as visible light harvesting and electron-generating centers. The LSPR-excited electrons would be enriched on the surface of the dewetted Ag nanoparticles. As a result, the electrons transferred from Ag to the CB of the adjacent semiconductor (WO$_3$ or CuO at the respective interface with Ag) and increased the steady-state concentration of "chemically useful" (i.e., charge carriers at the surface of the semiconductor that participated in photocatalytic reactions) energetic charge carriers.[60] In this study, the dispersed Ag nanoparticles were approximately 79 nm, implying that the quadrupolar LSPR could be the most probable mode in which photon absorption was predominant rather than hot carrier generation. As a result, the excess

electrons could also contribute to the production of more O$_2^{•−}$ (as shown in the schematic in Figure 9d). Bastús et al. and Seemala et al. reported that the Ag nanoparticle size and distribution greatly influenced the LSPR effect.[61,62] According to their reports, hot carrier generation was predominantly observed with relatively higher hot carrier density in relatively small Ag nanoparticles (∼67 nm), which exhibited dipolar plasmon resonance. Quadrupole moments could be observed above this critical size (∼67 nm), as the size of the Ag nanoparticle increased until ∼189 nm. This facilitated O$_2$ dissociation via direct interactions with the strong electric fields at the Ag surface due to the predominant photon absorption that effectively promoted photocatalysis.[62] Thus, the strong visible light absorption and charge separation ability of this Ag-dispersed CuO−WO$_3$ structure greatly enhanced the photocatalytic activity. Consequently, the Ag dispersion onto the fibers could remarkably improve the absorption of visible light due to the LSPR effect and significantly increased the probability of separation of charge carriers. Thus, the photogenerated electron−hole pairs were accompanied by the reduction/oxidation process for the degradation of the organic dye.

3. CONCLUSIONS

In summary, a novel and effective hybrid composite photocatalyst comprising a plasmonic metal (Ag)-dispersed CuO−WO$_3$ Z-scheme heterojunction was successfully coated on reusable and recyclable 3D network-like SGFs by an industrially well-adopted sputtering process. The XRD results revealed that the high concentration of Cu in 3Cu−WO$_3$ led to CuWO$_4$ phase formation at 873 K. Homogeneously dispersed,

localized surface diffusion-driven Ag-dewetted nanoparticles of approximately 79 nm were successfully obtained. The MB photocatalytic degradation efficiency of Ag-dispersed CuO−WO$_3$/SGF was about 18.6 times higher than that of pure WO$_3$-coated fibers. The construction of the Z-scheme hetero-junction system decreased the number of photogenerated electron−hole pairs. The dewetted Ag nanoparticle dispersion facilitated effective electron−hole transfer across the respective interfaces of Ag/CuO and Ag/WO$_3$, and it was certainly beneficial to retard the rapid recombination of electron holes from WO$_3$ and CuO. This work provides insights into the practical applications of highly efficient fiber-supported visible-light-active photocatalysts for environmental remediation.

4. EXPERIMENTAL SECTION

4.1. Fabrication of Cu−WO$_3$ and Ag-Dispersed CuO−WO$_3$ Photocatalysts on SGFs. A 3D network-like commercially available SGF sheet was used as a substrate for the deposition of WO$_3$ and Cu-doped WO$_3$ by radio frequency magnetron sputtering at room temperature. A 2 in. planar tungsten oxide target and a Cu chip (99.999% purity, chip size: $1 \times 1 \times 0.5$ mm)-embedded mosaic-type tungsten oxide target were used for the deposition of WO$_3$ and Cu−WO$_3$ over the SGF, respectively, under the same conditions. An Ar gas flow of 230 sccm, a target power of 150 W, a substrate rotation of 23 rpm, a target−substrate distance of 90 mm, and a deposition time of 30 min were maintained as deposition parameters. Before sputtering, the chamber was evacuated to a base pressure below 2×10^{-6} Torr and pre-sputtered for 10 min to remove any adsorbed contaminants on the surface of the sputter target. Finally, the WO$_3$ and Cu−WO$_3$-coated fibers were annealed at 873 K in ambient air for 30 min using the RTA system to obtain crystalline CuO−WO$_3$ composite nanostructures. The Cu concentration in the Cu−WO$_3$-coated fibers was controlled by the mosaic structure of the WO$_3$ target by varying the number of Cu chips (1, 2, and 3) on the WO$_3$ target, which were named as 1Cu−WO$_3$, 2Cu−WO$_3$, and 3Cu−WO$_3$, respectively. The Cu doping concentration was approximately 3−10 at. % based on the area fraction of Cu over the WO$_3$ target, respectively. Finally, an ultrathin Ag layer (∼10 nm) was sputtered over CuO−WO$_3$ (which was obtained by annealing 2Cu−WO$_3$ fibers annealed at 873 K) by the DC magnetron sputtering system using a 2 in. diameter Ag target of 99.999% purity with a target power supply of 30 W, and these fibers were subsequently annealed under vacuum for 5 min at 873 K to obtain Ag nanoparticle dispersion over the CuO−WO$_3$/SGF.

4.2. Material Characterization and Organic Dye Degradation. The crystal structure was examined by XRD with a Rigaku SmartLab X-ray diffractometer using Cu Kα radiation at a scanning speed of 4° min^{-1} over the 2θ range of 15−70°. The surface morphology was investigated using FE-SEM (TESCAN-MIRA3, Korea). XPS measurements were carried out with a Thermo Scientific K-Alpha spectrometer using an Al Kα X-ray source with a constant analyzer mode to study the chemical composition of the constituent elements. Raman measurements were carried out by HORIBA LabRAM HR-800 with 514 nm laser excitation. TEM observations were performed using an FEI TECNAI G2 F20 (operating voltage: 200 kV) to determine the structure and cross-sectional microstructure of the dewetted Ag nanoparticles dispersed on CuO−WO$_3$-coated fibers. The TEM sample was prepared by the H-bar technique using a TESCAN LYRA3 high-

resolution FIB-SEM. The optical absorbance spectra were recorded using a UV−vis−NIR spectrophotometer (UV-3600, Shimadzu). The PL properties were studied using a HORIBA LabRAM HR-800, HORIBA France SAS. The photocatalytic activity was investigated by measuring the degree of decomposition of MB solution in a double-walled glass beaker (40 mL MB solution, 10 ppm) under visible light illumination using a 500 W Xe lamp with a 400 nm filter.

■ ASSOCIATED CONTENT

Ⓢ Supporting Information

The Supporting Information is available free of charge at https://pubs.acs.org/doi/10.1021/acsomega.1c06239.

High-magnification FE-SEM images of as-coated WO$_3$ and Cu−WO$_3$ on SGFs, low-magnification FE-SEM image of Ag-dispersed CuO−WO$_3$/SGFs, evolution of the surface microstructure of the 10 nm-thick Ag film deposited (by magnetron sputtering) on glass substrates with respect to RTA temperature, photocatalytic stability test for three cycles, and the structure and morphology images of Ag-dispersed CuO−WO$_3$/SGFs after three cycles (PDF)

■ AUTHOR INFORMATION

Corresponding Author

Kee-Sun Lee − *Department of Advanced Materials Engineering & Smart Natural Space Research Center, Kongju National University, Cheonan 31080, Republic of Korea;* ⓞ orcid.org/0000-0003-4502-9782; Email: kslee@kongju.ac.kr

Author

Chadrasekhar Loka − *Department of Advanced Materials Engineering & Smart Natural Space Research Center, Kongju National University, Cheonan 31080, Republic of Korea;* ⓞ orcid.org/0000-0002-6802-8574

Complete contact information is available at:
https://pubs.acs.org/10.1021/acsomega.1c06239

Notes

The authors declare no competing financial interest.

■ ACKNOWLEDGMENTS

■ ABBREVIATIONS

LSPR, localized surface plasmon resonance; SGFs, silica glass fibers; XRD, X-ray diffraction; RF, radio frequency; RTA, rapid thermal annealing; FE-SEM, field-emission scanning electron microscopy; XPS, X-ray photoelectron spectroscopy; TEM, transmission electron microscopy; FIB-SEM, focused ion beam scanning electron microscopy; MB, methylene blue; HR-TEM, high-resolution transmission electron microscopy; FFT, fast Fourier transformation; IFFT, inverse fast Fourier transformation

■ REFERENCES

(1) Yoon, T. P.; Ischay, M. A.; Du, J. Visible Light Photocatalysis as a Greener Approach to Photochemical Synthesis. *Nat. Chem.* **2010**, *2*, 527−532.

(2) You, J.; Guo, Y.; Guo, R.; Liu, X. A Review of Visible Light-Active Photocatalysts for Water Disinfection: Features and Prospects. *Chem. Eng. J.* **2019**, *373*, 624−641.

(3) Yan, M.; Wu, Y.; Zhu, F.; Hua, Y.; Shi, W. The Fabrication of a Novel Ag 3 VO 4 /WO 3 Heterojunction with Enhanced Visible Light Efficiency in the Photocatalytic Degradation of TC. *Phys. Chem. Chem. Phys.* **2016**, *18*, 3308−3315.

(4) Bamwenda, G. R.; Arakawa, H. The Visible Light Induced Photocatalytic Activity of Tungsten Trioxide Powders. *Appl. Catal., A* **2001**, *210*, 181−191.

(5) Widiyandari, H.; Purwanto, A.; Balgis, R.; Ogi, T.; Okuyama, K. CuO/WO3 and Pt/WO3 Nanocatalysts for Efficient Pollutant Degradation Using Visible Light Irradiation. *Chem. Eng. J.* **2012**, *180*, 323−329.

(6) Weng, B.; Wu, J.; Zhang, N.; Xu, Y.-J. Observing the Role of Graphene in Boosting the Two-Electron Reduction of Oxygen in Graphene−WO 3 Nanorod Photocatalysts. *Langmuir* **2014**, *30*, 5574−5584.

(7) Murillo-Sierra, J. C.; Hernández-Ramírez, A.; Hinojosa-Reyes, L.; Guzmán-Mar, J. L. A Review on the Development of Visible Light-Responsive WO3-Based Photocatalysts for Environmental Applications. *Chem. Eng. J. Adv.* **2021**, *5*, 100070.

(8) Djurišić, A. B.; He, Y.; Ng, A. M. C. Visible-Light Photocatalysts: Prospects and Challenges. *APL Mater.* **2020**, *8*, 030903.

(9) Peleyeju, M. G.; Viljoen, E. L. WO3-Based Catalysts for Photocatalytic and Photoelectrocatalytic Removal of Organic Pollutants from Water − A Review. *J. Water Process Eng.* **2021**, *40*, 101930.

(10) Li, H.; Zhou, Y.; Tu, W.; Ye, J.; Zou, Z. State-of-the-Art Progress in Diverse Heterostructured Photocatalysts toward Promoting Photocatalytic Performance. *Adv. Funct. Mater.* **2015**, *25*, 998−1013.

(11) Yuan, X.; Jiang, L.; Chen, X.; Leng, L.; Wang, H.; Wu, Z.; Xiong, T.; Liang, J.; Zeng, G. Highly Efficient Visible-Light-Induced Photoactivity of Z-Scheme Ag 2 CO 3 /Ag/WO 3 Photocatalysts for Organic Pollutant Degradation. *Environ. Sci.: Nano* **2017**, *4*, 2175−2185.

(12) Wang, W.; Yang, R.; Li, T.; Komarneni, S.; Liu, B. Advances in Recyclable and Superior Photocatalytic Fibers: Material, Construction, Application and Future Perspective. *Composites, Part B* **2021**, *205*, 108512.

(13) Fukugaichi, S. Fixation of Titanium Dioxide Nanoparticles on Glass Fiber Cloths for Photocatalytic Degradation of Organic Dyes. *ACS Omega* **2019**, *4*, 15175−15180.

(14) Heo, K. J.; Jeong, S. B.; Shin, J.; Hwang, G. B.; Ko, H. S.; Kim, Y.; Choi, D. Y.; Jung, J. H. Water-Repellent TiO 2 -Organic Dye-Based Air Filters for Efficient Visible-Light-Activated Photochemical Inactivation against Bioaerosols. *Nano Lett.* **2021**, *21*, 1576−1583.

(15) Preston, A. S.; Hughes, R. A.; Demille, T. B.; Rey Davila, V. M.; Neretina, S. Dewetted Nanostructures of Gold, Silver, Copper, and Palladium with Enhanced Faceting. *Acta Mater.* **2019**, *165*, 15−25.

(16) Gellé, A.; Price, G. D.; Voisard, F.; Brodusch, N.; Gauvin, R.; Amara, Z.; Moores, A. Enhancing Singlet Oxygen Photocatalysis with Plasmonic Nanoparticles. *ACS Appl. Mater. Interfaces* **2021**, *13*, 35606−35616.

(17) Yoshikawa, H.; Hironou, A.; Shen, Z.; Tamiya, E. Versatile Micropatterning of Plasmonic Nanostructures by Visible Light Induced Electroless Silver Plating on Gold Nanoseeds. *ACS Appl. Mater. Interfaces* **2016**, *8*, 23932−23940.

(18) Demille, T. B.; Hughes, R. A.; Neretina, S. Periodic Arrays of Dewetted Silver Nanostructures on Sapphire and Quartz: Effect of Substrate Truncation on the Localized Surface Plasmon Resonance and Near-Field Enhancement. *J. Phys. Chem. C* **2019**, *123*, 19879−19886.

(19) Liang, Y.-C.; Wang, C.-C.; Kei, C.-C.; Hsueh, Y.-C.; Cho, W.-H.; Perng, T.-P. Photocatalysis of Ag-Loaded TiO 2 Nanotube Arrays Formed by Atomic Layer Deposition. *J. Phys. Chem. C* **2011**, *115*, 9498−9502.

(20) Zhang, Z.; Wang, W.; Gao, E.; Sun, S.; Zhang, L. Photocatalysis Coupled with Thermal Effect Induced by SPR on Ag-Loaded Bi 2 WO 6 with Enhanced Photocatalytic Activity. *J. Phys. Chem. C* **2012**, *116*, 25898−25903.

(21) Scuderi, M.; Esposito, M.; Todisco, F.; Simeone, D.; Tarantini, I.; De Marco, L.; De Giorgi, M.; Nicotra, G.; Carbone, L.; Sanvitto, D.; Passaseo, A.; Gigli, G.; Cuscunà, M. Nanoscale Study of the Tarnishing Process in Electron Beam Lithography-Fabricated Silver Nanoparticles for Plasmonic Applications. *J. Phys. Chem. C* **2016**, *120*, 24314−24323.

(22) Deng, J.; He, S.; Xie, S.; Yang, H.; Liu, Y.; Guo, G.; Dai, H. Ultralow Loading of Silver Nanoparticles on Mn 2 O 3 Nanowires Derived with Molten Salts: A High-Efficiency Catalyst for the Oxidative Removal of Toluene. *Environ. Sci. Technol.* **2015**, *49*, 11089−11095.

(23) Zhou, M.; Li, J.; Ye, Z.; Ma, C.; Wang, H.; Huo, P.; Shi, W.; Yan, Y. Transfer Charge and Energy of Ag@CdSe QDs-RGO Core−Shell Plasmonic Photocatalyst for Enhanced Visible Light Photo-catalytic Activity. *ACS Appl. Mater. Interfaces* **2015**, *7*, 28231−28243.

(24) Thompson, C. V. Solid-State Dewetting of Thin Films. *Annu. Rev. Mater. Res.* **2012**, *42*, 399−434.

(25) Quan, J.; Zhang, J.; Qi, X.; Li, J.; Wang, N.; Zhu, Y. A Study on the Correlation between the Dewetting Temperature of Ag Film and SERS Intensity. *Sci. Rep.* **2017**, *7*, 14771.

(26) Oh, H.; Pyatenko, A.; Lee, M. A Hybrid Dewetting Approach to Generate Highly Sensitive Plasmonic Silver Nanoparticles with a Narrow Size Distribution. *Appl. Surf. Sci.* **2021**, *542*, 148613.

(27) Shi, R.; Zhang, Z.; Luo, F. N-Doped Graphene-Based CuO/WO3/Cu Composite Material with Performances of Catalytic Decomposition 4-Nitrophenol and Photocatalytic Degradation of Organic Dyes. *Inorg. Chem. Commun.* **2020**, *121*, 108246.

(28) Bajiri, M. A.; Hezam, A.; Namratha, K.; Viswanath, R.; Drmosh, Q. A.; Bhojya Naik, H. S.; Byrappa, K. CuO/ZnO/g-C3N4 Heterostructures as Efficient Visible Light-Driven Photocatalysts. *J. Environ. Chem. Eng.* **2019**, *7*, 103412.

(29) Xie, Y. P.; Liu, G.; Yin, L.; Cheng, H.-M. Crystal Facet-Dependent Photocatalytic Oxidation and Reduction Reactivity of Monoclinic WO3 for Solar Energy Conversion. *J. Mater. Chem.* **2012**, *22*, 6746.

(30) Kalanur, S. S.; Seo, H. Directing WO3 Crystal Growth towards Artificial Photosynthesis Favorable {002} Plane via Aluminum Incorporation in the Lattice for Enhanced Water Splitting. *J. Alloys Compd.* **2021**, *864*, 158186.

(31) Figueiredo, V.; Elangovan, E.; Gonçalves, G.; Barquinha, P.; Pereira, L.; Franco, N.; Alves, E.; Martins, R.; Fortunato, E. Effect of Post-Annealing on the Properties of Copper Oxide Thin Films Obtained from the Oxidation of Evaporated Metallic Copper. *Appl. Surf. Sci.* **2008**, *254*, 3949−3954.

(32) Choudhary, S.; Sarma, J. V. N.; Pande, S.; Ababou-Girard, S.; Turban, P.; Lepine, B.; Gangopadhyay, S. Oxidation Mechanism of Thin Cu Films: A Gateway towards the Formation of Single Oxide Phase. *AIP Adv.* **2018**, *8*, 055114.

(33) Polyakov, B.; Kuzmin, A.; Vlassov, S.; Butanovs, E.; Zideluns, J.; Butikova, J.; Kalendarev, R.; Zubkins, M. A Comparative Study of Heterostructured CuO/CuWO4 Nanowires and Thin Films. *J. Cryst. Growth* **2017**, *480*, 78−84.

(34) Wen, Z.; Wu, W.; Liu, Z.; Zhang, H.; Li, J.; Chen, J. Ultrahigh-Efficiency Photocatalysts Based on Mesoporous Pt−WO3 Nano-hybrids. *Phys. Chem. Chem. Phys.* **2013**, *15*, 6773.

(35) Li, S.; Yao, Z.; Zhou, J.; Zhang, R.; Shen, H. Fabrication and Characterization of WO3 Thin Films on Silicon Surface by Thermal Evaporation. *Mater. Lett.* **2017**, *195*, 213−216.

(36) Xie, F. Y.; Gong, L.; Liu, X.; Tao, Y. T.; Zhang, W. H.; Chen, S. H.; Meng, H.; Chen, J. XPS Studies on Surface Reduction of

Tungsten Oxide Nanowire Film by Ar + Bombardment. *J. Electron Spectrosc. Relat. Phenom.* **2012**, *185*, 112−118.

(37) Thongpan, W.; Louloudakis, D.; Pooseekheaw, P.; Kumpika, T.; Kantarak, E.; sroila, W.; Panthawan, A.; Thongsuwan, W.; Singjai, P. Porous CuWO4/WO3 Composite Films with Improved Electrochromic Properties Prepared by Sparking Method. *Mater. Lett.* **2019**, *257*, 126747.

(38) Ramgir, N. S.; Goyal, C. P.; Sharma, P. K.; Goutam, U. K.; Bhattacharya, S.; Datta, N.; Kaur, M.; Debnath, A. K.; Aswal, D. K.; Gupta, S. K. Selective H2S Sensing Characteristics of CuO Modified WO3 Thin Films. *Sens. Actuators, B* **2013**, *188*, 525−532.

(39) Suryawanshi, S. R.; Singh, A. K.; Deo, M.; Late, D. J.; Sinha, S.; More, M. A. 3D Hetero-Architecture of GdB 6 Nanoparticles on Lessened Cubic Cu 2 O Nanowires: Enhanced Field Emission Behaviour. *CrystEngComm* **2015**, *17*, 3936−3944.

(40) Ling, P.; Zhang, Q.; Cao, T.; Gao, F. Versatile Three-Dimensional Porous Cu@Cu 2 O Aerogel Networks as Electrocatalysts and Mimicking Peroxidases. *Angew. Chem.* **2018**, *130*, 6935−6940.

(41) Wang, K.; Dong, X.; Zhao, C.; Qian, X.; Xu, Y. Facile Synthesis of Cu2O/CuO/RGO Nanocomposite and Its Superior Cyclability in Supercapacitor. *Electrochim. Acta* **2015**, *152*, 433−442.

(42) Biesinger, M. C.; Hart, B. R.; Polack, R.; Kobe, B. A.; Smart, R. S. C. Analysis of Mineral Surface Chemistry in Flotation Separation Using Imaging XPS. *Miner. Eng.* **2007**, *20*, 152−162.

(43) Biesinger, M. C. Advanced Analysis of Copper X-Ray Photoelectron Spectra. *Surf. Interface Anal.* **2017**, *49*, 1325−1334.

(44) Lima, A. E. B.; Reis, R. Y. N.; Ribeiro, L. S.; Ribeiro, L. K.; Assis, M.; Santos, R. S.; Fernandes, C. H. M.; Cavalcante, L. S.; Longo, E.; Osajima, J. A. O.; Luz, G. E. Microwave-Assisted Hydrothermal Synthesis of CuWO4-Palygorskite Nanocomposite for Enhanced Visible Photocatalytic Response. *J. Alloys Compd.* **2021**, *863*, 158731.

(45) Tian, C. M.; Jiang, M.; Tang, D.; Qiao, L.; Xiao, H. Y.; Oropeza, F. E.; Hofmann, J. P.; Hensen, E. J. M.; Tadich, A.; Li, W.; Qi, D. C.; Zhang, K. H. L. Elucidating the Electronic Structure of CuWO4 Thin Films for Enhanced Photoelectrochemical Water Splitting. *J. Mater. Chem. A* **2019**, *7*, 11895−11907.

(46) Wang, L.; Rehman, A. U.; Wu, H.; Wu, B.; Li, L.; Shi, K. Submicrochains Composed of Massage Ball-like WO 3 @CuWO 4 Composites for High-Efficiency CO Gas Sensing Applications at Room Temperature. *RSC Adv.* **2016**, *6*, 69999−70007.

(47) Zhu, W.; Liu, J.; Yu, S.; Zhou, Y.; Yan, X. Ag Loaded WO3 Nanoplates for Efficient Photocatalytic Degradation of Sulfanilamide and Their Bactericidal Effect under Visible Light Irradiation. *J. Hazard. Mater.* **2016**, *318*, 407−416.

(48) Gholami, P.; Khataee, A.; Bhatnagar, A.; Vahid, B. Synthesis of N-Doped Magnetic WO3- X@Mesoporous Carbon Using a Diatom Template and Plasma Modification: Visible-Light-Driven Photocatalytic Activities. *ACS Appl. Mater. Interfaces* **2021**, *13*, 13072−13086.

(49) Roshani, R.; Tadjarodi, A. Preparation of Nanocomposite with Different Component Ratios of CuWO4 Nanoparticles and Nitrogen-Doped Reduced Graphene Oxide to Compare Their Supercapacitive Properties. *J. Alloys Compd.* **2021**, *856*, 157302.

(50) Gajraj, V.; Mariappan, C. R. CuWO4: A Promising Multifunctional Electrode Material for Energy Storage as in Redox Active Solid-State Asymmetric Supercapacitor and an Electrocatalyst for Energy Conversion in Methanol Electro-Oxidation. *J. Electroanal. Chem.* **2021**, *895*, 115504.

(51) Quyen, V. T.; Kim, J.; Park, P.-M.; Huong, P. T.; Viet, N. M.; Thang, P. Q. Enhanced the Visible Light Photocatalytic Decomposition of Antibiotic Pollutant in Wastewater by Using Cu Doped WO3. *J. Environ. Chem. Eng.* **2021**, *9*, 104737.

(52) Lima, A. E. B.; Costa, M. J. S.; Santos, R. S.; Batista, N. C.; Cavalcante, L. S.; Longo, E.; Luz, G. E. Facile Preparation of CuWO4 Porous Films and Their Photoelectrochemical Properties. *Electrochim. Acta* **2017**, *256*, 139−145.

(53) Raizada, P.; Sharma, S.; Kumar, A.; Singh, P.; Parwaz Khan, A. A.; Asiri, A. M. Performance Improvement Strategies of CuWO4 Photocatalyst for Hydrogen Generation and Pollutant Degradation. *J. Environ. Chem. Eng.* **2020**, *8*, 104230.

(54) Yaghoot-Nezhad, A.; Moradi, M.; Rostami, M.; Danaee, I.; Khosravi-Nikou, M. R. Dual Z-Scheme CuO-ZnO@Graphitic Carbon Nitride Ternary Nanocomposite with Improved Visible Light-Induced Catalytic Activity for Ultrasound-Assisted Photocatalytic Desulfurization. *Energy Fuels* **2020**, *34*, 13588−13605.

(55) Gong, H.; Ma, R.; Mao, F.; Liu, K.; Cao, H.; Yan, H. Light-Induced Spatial Separation of Charges toward Different Crystal Facets of Square-like WO 3. *Chem. Commun.* **2016**, *52*, 11979−11982.

(56) Wang, S.; Chen, H.; Gao, G.; Butburee, T.; Lyu, M.; Thaweesak, S.; Yun, J.-H.; Du, A.; Liu, G.; Wang, L. Synergistic Crystal Facet Engineering and Structural Control of WO3 Films Exhibiting Unprecedented Photoelectrochemical Performance. *Nano Energy* **2016**, *24*, 94−102.

(57) Yourey, J. E.; Pyper, K. J.; Kurtz, J. B.; Bartlett, B. M. Chemical Stability of CuWO 4 for Photoelectrochemical Water Oxidation. *J. Phys. Chem. C* **2013**, *117*, 8708−8718.

(58) Sahu, K.; Bisht, A.; Pandey, A.; Dutta, A.; Khan, S. A.; Singhal, R.; Som, T.; Mohapatra, S. RF Magnetron Sputtered Ag-Cu2O-CuO Nanocomposite Thin Films with Highly Enhanced Photocatalytic and Catalytic Performance. *Appl. Surf. Sci.* **2020**, *517*, 146169.

(59) Pandey, P.; Kunwar, S.; Sui, M.; Bastola, S.; Lee, J. Compositional Effect on the Fabrication of Ag x Pd 1−x Alloy Nanoparticles on c -Plane Sapphire at Distinctive Stages of the Solid-State-Dewetting of Bimetallic Thin Films. *RSC Adv.* **2017**, *7*, 55471−55481.

(60) Linic, S.; Christopher, P.; Ingram, D. B. Plasmonic-Metal Nanostructures for Efficient Conversion of Solar to Chemical Energy. *Nat. Mater.* **2011**, *10*, 911−921.

(61) Bastús, N. G.; Piella, J.; Puntes, V. Quantifying the Sensitivity of Multipolar (Dipolar, Quadrupolar, and Octapolar) Surface Plasmon Resonances in Silver Nanoparticles: The Effect of Size, Composition, and Surface Coating. *Langmuir* **2016**, *32*, 290−300.

(62) Seemala, B.; Therrien, A. J.; Lou, M.; Li, K.; Finzel, J. P.; Qi, J.; Nordlander, P.; Christopher, P. Plasmon-Mediated Catalytic O 2 Dissociation on Ag Nanostructures: Hot Electrons or Near Fields? *ACS Energy Lett.* **2019**, *4*, 1803−1809.